

MATERIALS SCIENCE

The existence and impact of persistent ferroelectric domains in MAPbI₃

Lauren M. Garten^{1*}, David T. Moore¹, Sanjini U. Nanayakkara¹, Shyam Dwaraknath², Philip Schulz^{1,3}, Jake Wands⁴, Angus Rockett⁴, Brian Newell⁵, Kristin A. Persson^{2,6}, Susan Trolier-McKinstry⁷, David S. Ginley^{1*}

Methylammonium lead iodide (MAPbI₃) exhibits exceptional photovoltaic performance, but there remains substantial controversy over the existence and impact of ferroelectricity on the photovoltaic response. We confirm ferroelectricity in MAPbI₃ single crystals and demonstrate mediation of the electronic response by ferroelectric domain engineering. The ferroelectric response sharply declines above 57°C, consistent with the tetragonal-to-cubic phase transition. Concurrent band excitation piezoresponse force microscopy–contact Kelvin probe force microscopy shows that the measured response is not dominated by spurious electrostatic interactions. Large signal poling (>16 V/cm) orients the permanent polarization into large domains, which show stabilization over weeks. X-ray photoemission spectroscopy results indicate a shift of 400 meV in the binding energy of the iodine core level peaks upon poling, which is reflected in the carrier concentration results from scanning microwave impedance microscopy. The ability to control the ferroelectric response provides routes to increase device stability and photovoltaic performance through domain engineering.

INTRODUCTION

Ferroelectric semiconductors have the potential to enable photovoltaic performance not possible in other materials; ferroelectric polarization enables charge separation, allows for the design of the electrical response, and has the potential to exceed the Shockley-Queisser limit through the bulk photovoltaic effect (1, 2). However, classic ferroelectric materials typically have large bandgaps and thus would not be effective as solar energy absorbers. Here, we show that MAPbI₃, with a near ideal bandgap of 1.6 eV and verified solar cell efficiency over 19% (3), is ferroelectric. We probe single crystals with small-signal electrical measurements and cutting-edge scanning probe techniques to confirm ferroelectricity in MAPbI₃. Single crystals serve as a model system allowing a probing of the fundamental mechanisms and a complete set of data by a variety of approaches to confirm the ferroelectric response and simultaneously avoid any potential measurement artifacts arising from a nonstoichiometric secondary phase or grain boundaries, which might be present in thin film samples. The characterization techniques used to confirm the ferroelectric response included d₃₃ Berlincourt piezoelectric measurements, band excitation piezoresponse force microscopy with concurrent contact Kelvin probe force microscopy (BE-PFM/cKPFM), single-frequency piezoresponse force microscopy (PFM), temperature-dependent Rayleigh analysis, and electric force microscopy (EFM). After identifying a ferroelectric response and determining the conditions for macroscopic domain control, the impact of poling on the material stability and electrical response were measured through EFM, scanning microwave impedance microscopy (sMIM), and x-ray photoemission spectroscopy (XPS).

¹National Renewable Energy Laboratory, Golden, CO 80401, USA. ²Lawrence Berkeley National Laboratory, 1 Cyclotron Rd, Berkeley, CA 94720, USA. ³CNRS, Institut Photovoltaïque d'Île de France, UMR 9006, 30 route départementale 128, Palaiseau 91120, France. ⁴Colorado School of Mines, Golden, CO 80401, USA. ⁵Colorado State University, Fort Collins, CO 80523, USA. ⁶University of California, Berkeley, Berkeley, CA 94704, USA. ⁷The Pennsylvania State University, University Park, PA 16802, USA.
*Corresponding author. Email: david.ginley@nrel.gov (D.S.G.); lmg356@gmail.com (L.M.G.)

There are two critical requirements for ferroelectricity: the material must have a spontaneous polarization, which forms upon going through a paraelectric-to-ferroelectric phase transition, and that polarization must be reorientable along at least two directions with an applied electric field (4). Frequently, the ability to change the direction of the polarization is probed by some combination of PFM and polarization-electric field (PE) loops. These traditional techniques are appropriate under the condition that the measured charge is principally due to the intrinsic polarization of the material and that the electronic and the ionic contributions are negligible. However, as the material becomes more semiconducting (increasing the possibility of electronic contributions) and its lattice becomes more plastic (allowing ion motion), the application of traditional techniques becomes difficult or impossible. MAPbI₃ is a semiconductor with a very plastic lattice and is, as we will show here, ferroelectric. This highlights the need for a definitive determination of ferroelectricity that will require the use of techniques capable of detecting ferroelectricity in materials with large electronic and ionic contributions to conductivity. This work elucidates the ferroelectric response in these materials, sheds light on the contradictory reports of ferroelectricity, and shows the mediation of the domain and, thus, electrical response through domain engineering.

RESULTS

Piezoelectricity is a prerequisite of ferroelectricity and is easier to detect using direct, macroscopic measurements. Here, the d₃₃ piezoelectric coefficient is measured using a Berlincourt meter. Berlincourt measurements use the application of a symmetric axial strain to the crystal to generate a current in the sample through the piezoelectric effect. No electric field is applied during this measurement, only a symmetric axial strain, which would not drive free charge or ion migration. Prior to the application of an electric field, no piezoelectric response could be measured in our samples. When a material is ferroelectric, it can have the polarization oriented along multiple directions. To see a macroscopic piezoelectric response, the polarization

Copyright © 2019
The Authors, some
rights reserved;
exclusive licensee
American Association
for the Advancement
of Science. No claim to
original U.S. Government
Works. Distributed
under a Creative
Commons Attribution
NonCommercial
License 4.0 (CC BY-NC).

Downloaded from <http://advances.sciencemag.org/> on June 17, 2019

must be aligned predominately along one direction so that there is a macroscopic broken center of symmetry. To align the polarization along one direction, we use an electric field (termed “poling”). The samples are poled for 5 min at 21 V/cm. Five minutes after poling, d_{33} was found to be 54 pC/N. The measured value is in good agreement with the value calculated by density functional theory (DFT) of 32.8 pC/N (see the Supplementary Materials for details on DFT calculations). This confirms that MAPbI₃ is piezoelectric, that is, it exhibits a non-centrosymmetric structure at room temperature. Observing a piezoelectric response after poling is consistent with ferroelectricity. To further determine that this response is due to ferroelectricity, we investigated polarization response to an applied electric field.

As noted above, decoupling the electronic, ionic, and dipolar effects in MAPbI₃ is not trivial due to the electronic and ionic contributions to conductivity. Therefore, we use BE-PFM/cKPFM to show that MAPbI₃ is ferroelectric and that the response is predominately from the ferroelectric polarization. BE-PFM/cKPFM is the current state of the art, which has previously been shown to differentiate between ferroelectric (electromechanical) and electrostatic contributions to ferroelectric hysteresis (5).

The cKPFM response is consistent with the presence of an intrinsic ferroelectric polarization in the crystal and that the polarization is switchable by an external field. The cKPFM protocol, described further in the Supplementary Materials, uses DC pulses (write steps, V_{write}) to change the functional response (e.g., due to ferroelectric switching) and the application of a subsequent smaller DC voltage (read step, V_{read}) to track the changes in electrostatic forces. Figure 1A shows an image of an as-grown MAPbI₃ single crystal prior to electrical measurements. Figure 1B shows a schematic of the write steps (and subsequent read steps) taken using a 10× amplifier from 0 to 15 V, then 15 to −15 V, and then −15 to 0 V with read steps from −2 to 2 V. A schematic of the read and write voltage steps is shown in fig. S2A, with the cKPFM data only from the maximum positive to maximum negative write voltage for a single point, single measurement in fig. S2B. The resulting cKPFM as a function of read step for a series of poling (write) voltages is shown in Fig. 1C. With increasing positive write voltage from 0 to 15 V, indicated by the color scale, the sample is poled into a predominately positive domain orientation, which is maintained as the voltage is then decreased (from 15 to 0 V), creating a band of constant response. This process is then repeated as the sample is poled in the opposite direction, creating two discrete bands each offset equally from the origin, indicating that there are two discrete switchable polarization states (ferroelectricity). Figure 1C shows a saturation of the y intercept as the intrinsic polarization saturates and the electrostatic contributions appear negligible in comparison. In addition, the cKPFM response as a function of read voltage is nearly horizontal, indicating little electrostatic contribution.

During the cKPFM read and write steps, the periodic tip oscillations are monitored in band excitation PFM mode. In BE-PFM, an AC excitation voltage with a band of frequencies centered around the contact resonance frequency is applied to track voltage-induced changes in functional response. By tracking the full resonance response, BE-PFM avoids the issues that plague single-frequency PFM, where changes in tip, e.g., variation in sample contact stiffness, can be mistaken as a change in the piezoelectric response (6). The frequency-dependent BE-PFM response is fit to a simple harmonic oscillator model, from which the oscillation amplitude, phase, resonance frequency, and quality factor are extracted. Raw amplitude

and phase spectrograms for a single-point measurement are shown in fig. S1 (A and B), and a schematic of the write steps (−15 to 15 V) and read steps (−2 to 2 V) made during the BE-PFM/cKPFM measurements is shown in fig. S1C. Figure 1D is the average off-field response for all read steps (where the y axis response is the amplitude x cosine of the phase). Figure 1E shows the average on-field loop (taken during the application of the write DC voltage). The pure PFM response comes from the cKPFM measurements taken at 0 V_{read} . The piezoresponse taken as the average of 10 measurements taken over 10 locations on the sample is shown in fig. S3. The observed functional response is consistent with ferroelectric hysteresis due to polarization switching, with a coercive voltage of approximately 3.5 to 4.0 V. The sharpness of these hysteresis loops and the minimal difference between the initial and final polarization indicate low injected charge during cycling; thus, the response is not dominated by surface charge. This finding is further supported by the sMIM data, discussed below, which show a modest change in carrier density and net carrier type (i.e., Fermi level) across domains. In the present study, the BE-PFM/cKPFM data confirm that this response is predominantly due to the intrinsic polarization and shows the switching of this polarization with an applied electric field.

The ferroelectric response is further corroborated by single-frequency PFM amplitude and phase as a function of applied V_{DC} (shown in fig. S4). These measurements are taken on fresh crystals prior to any poling voltage being applied. Notably, the offset in both the amplitude and phase data between the trace and retrace is much smaller than typical ferroelectrics, which is consistent with relaxor ferroelectricity. Relaxor ferroelectrics have a spontaneous polarization, which orders into nanoscale polar regions typically associated with regions of nanoscale chemical inhomogeneity (7). Given these results, the offset minimum in the forward and reverse sweeps, the linear displacement with applied field, and the hysteresis in trace and retrace can be assigned to a piezoelectric (rather than a pure electrostrictive) response associated with the reorientation of ferroelectric domains by an electric field. The concomitant phase shift of 180° is also indicative of a ferroelectric domain reversal.

Taken in concert, the BE-PFM/cKPFM and PFM data show that this material fulfills the criteria of ferroelectricity, a spontaneous polarization that can be reoriented with the application of an electric field. To further corroborate these results, we have also used advanced alternative methodologies based on Rayleigh analysis. The Rayleigh response is the linear change in permittivity under an applied electric field, E_{AC} , due to the irreversible movement of domain walls, domain clusters, or phase boundaries. (8). Rayleigh analysis has been used as an indicator for the presence of ferroelectric domain wall movement with a Gaussian distribution of restoring forces. Figure 2A shows the E_{AC} -induced dielectric response measured under small-signal conditions (<8.3 V/cm, <2 V) at 1 MHz with increasing temperature. The Rayleigh coefficient and concurrent loss are shown in fig. S4 (A and B). A clear Rayleigh response is apparent in MAPbI₃, indicating ferroelectric polar clusters, with mobile boundaries. The movement of the boundary between two ferroelectric domains (areas where the polarization is oriented along the same direction) in this case comes from the switching of the polarization orientation in the areas at or near that boundary due to the applied electric field.

The AC electric field dispersion, the Rayleigh response, decays with increasing temperature, sharply declining near 57°C, and, lastly, disappearing beyond 75°C. The transition near 57°C is consistent

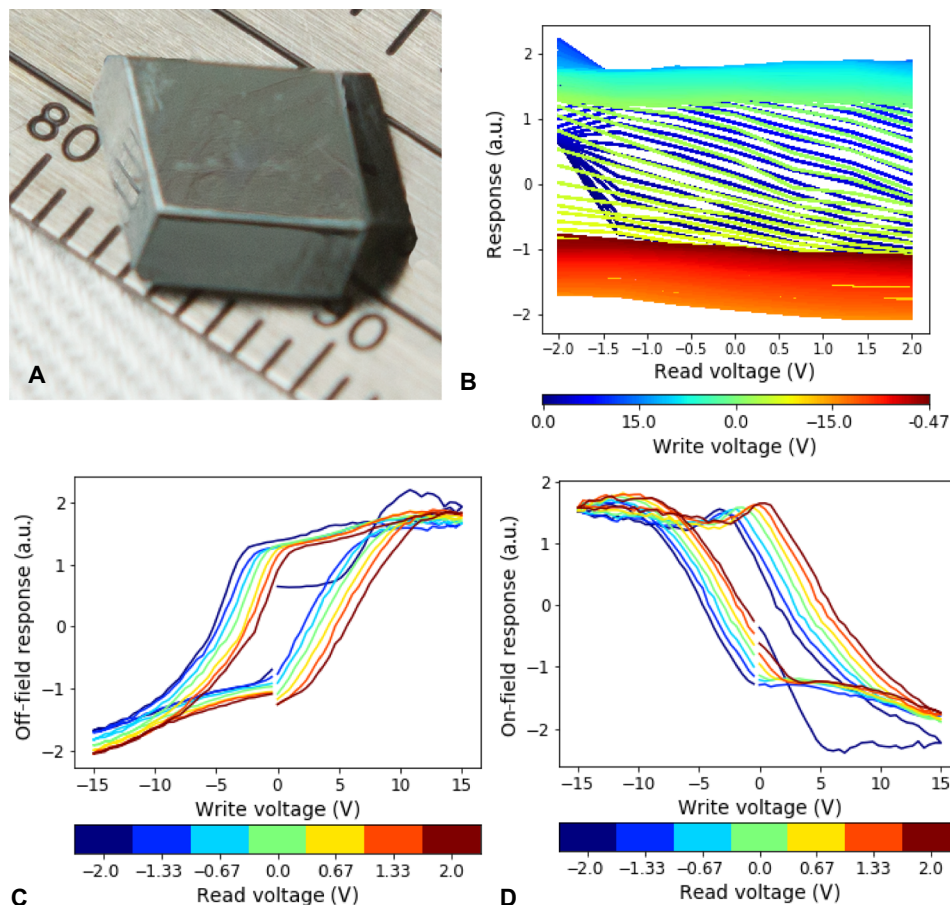


Fig. 1. Band excitation piezoresponse force microscopy with contact Kelvin probe force microscopy. (A) Image of an as-grown single crystal of MAPbI₃ with natural faceting. (B) The cKPFM response as a function of read voltage for a number of write voltages indicated by color. (C) The averaged BE-PFM off-field response and subsequent write steps as a function of applied DC write voltage. (D) The averaged BE-PFM on-field response and subsequent write steps as a function of applied DC write voltage. a.u., arbitrary units.

with previous reports of the temperature of transition between the tetragonal and cubic phases between 60° and 65°C (9). Figure 2B shows the transition temperatures for the paraelectric (cubic) phase to the ferroelectric (tetragonal) phase compared with the temperature range of the Rayleigh response. The consistency of the transition to the Rayleigh response and the fact that the AC electric field dispersion (the Rayleigh response) and dielectric loss tangent decrease with increasing temperature exclude ion motion as the sole origin of the response. The Rayleigh coefficient, shown in fig. S4, was calculated from the slope of the AC electric field dependence of the permittivity. There are many contributions to the loss in these materials leading to a convoluted response, but if only space-charge mechanisms were present, then the permittivity and loss tangent should increase with temperature. The fact that the permittivity decreases as the temperature increases is consistent with ferroelectricity (4). This is also consistent with the loss of dispersion in the permittivity data above approximately 57°C.

The persistence of the Rayleigh response beyond the global phase transition temperature, taken with the narrow hysteresis in the spontaneous polarization (PFM data above), implies that MAPbI₃ is a relaxor ferroelectric. The nanoscale regions of local polarity in relaxor ferroelectrics can be randomly oriented (the bulk polarization being the spatial/temporal average of all domains), and some

can persist above the global phase transition temperature (8). This effect gives rise to narrow hysteresis loops, a persistent Rayleigh response above the macroscopic phase transition temperature, frequency dispersion in the dielectric temperature dependence, which collapses above the macroscopic transition temperature, and the ability to induce a macroscopic ferroelectric response with applied electric field (7). All of these characteristics are shown here.

In addition to demonstrating that single-crystal MAPbI₃ exhibits ferroelectric behavior across many measurement modalities, the ability to pole the material into persistent macroscopic domains indicates that domain engineering can be used to select for a desired predominant polarization orientation and, thus, control the structure and electronic response. After removing the applied bias, large visible domain structures remained. Periodic domain structures extended millimeters across the surface of the samples, with domain widths that varied with poling field and orientation, ranging from approximately 2 to 40 μm (shown in Fig. 2C). An image of the crystal surface prior to poling is shown in fig. S5. It should also be stressed that the use of the term “persistent” here is to stress that the ferroelectricity does not disappear over time. The domain walls can move due to the switching of a few unit cells near the walls under applied electric field so that one area of polarization will grow at the expense of another but the material is still ferroelectric.

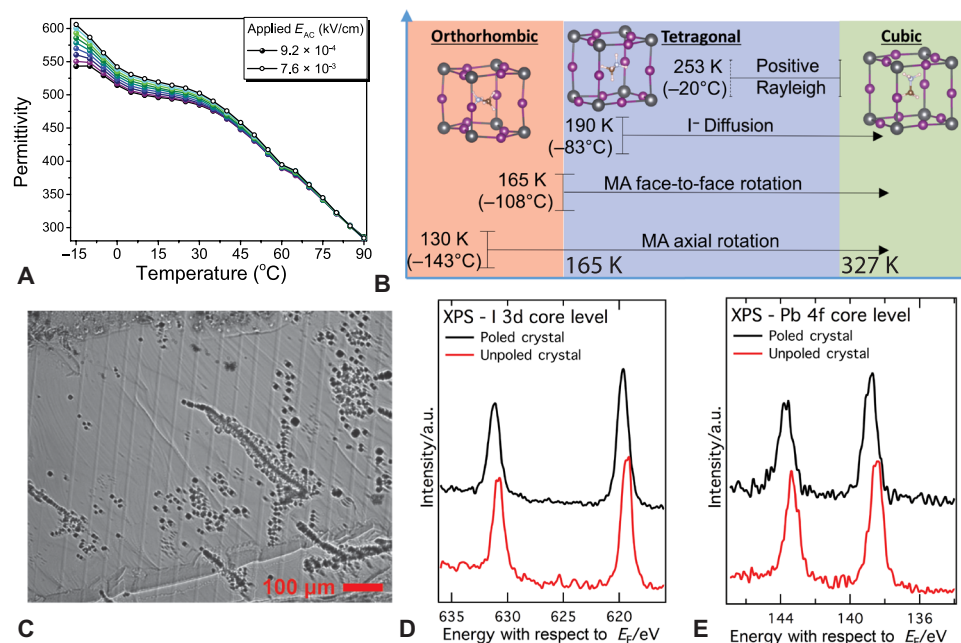


Fig. 2. The ferroelectric response as a function of electric field and temperature and the impact of poling-induced macroscopic ferroelectric domains. (A) The Rayleigh response, determined from the E_{AC} dependence of the permittivity measured at 1 MHz, from the lowest applied signal (black) increasing with applied voltage to the maximum (open), collapses near the global phase transition temperature for the cubic phase. (B) A schematic of the material structure, the temperature dependence of the global phase transitions, possible mechanisms of structural modification, and Rayleigh response in MAPbI_3 . (C) Optical microscope image of crystal surface after poling showing stable periodic domain lines that extend across the face of the crystal. (D) XPS measurements showing the energy with respect to E_F of the I 3d core level region. (E) XPS measurement showing the energy with respect to E_F of the Pb 4f core level region.

In inorganic, oxide-based perovskite, ferroelectric domains have been shown to affect both charge transport and interfacial chemistry (10). Therefore, with the ability to control the ferroelectric domain structure on a macroscopic scale comes the potential to affect the electronic performance, which is postulated for this material and demonstrated in other systems (11). XPS was therefore used to examine the impact of ferroelectricity. The iodine and lead core level spectra of a poled and unpoled MAPbI_3 crystal are depicted in Fig. 2 (D and E). For the unpoled crystal, the main I 3d_{5/2} peak is centered at 619.3 eV, which is consistent with an intrinsic response (12, 13). Relative to the measurements taken on an unpoled crystal, the iodine core level peaks in the poled crystal exhibit a rigid shift in binding energy of 400 meV with a similar shift in the Pb 4f peaks (see Table 1). This change in Fermi level, E_F , directly relates to the average change in surface polarization. A photoelectron escaping the solid has an energy that is the sum of the unpoled escape energy and the surface polarization energy. In this case, the shift is toward a higher binding energy, indicating that the surface is positively charged. In this analysis, we expect core level shifts in the opposite direction for opposite poling. This suggests that charge separation in and charge carrier collection from MAPbI_3 in a photovoltaic device could be altered by poling.

The impact of ferroelectric domains in MAPbI_3 was further probed by sMIM. Figure 3 (A to C) show the topography, sMIM amplitude, and sMIM phase, respectively. The image was acquired on an area that exhibited multiple domain orientations after negative poling of the sample. All three images show the presence of domains clearly. The domain visible in the images is consistent with the domains shown in Fig. 2C. The increase in dC/dV amplitude suggests a lower carrier concentration within the positive domain.

Table 1. Centroid positions of lead and iodine core level peaks before and after poling.

	Unpoled	Poled
I 3d _{5/2}	619.3 eV	619.7 eV
I 3d _{3/2}	630.8 eV	631.2 eV
Pb 4f _{7/2}	138.5 eV	138.9 eV
Pb 4f _{5/2}	143.3 eV	143.7 eV

In addition, the decrease in dC/dV phase corresponds to behavior that is more n-type, which is in agreement with the increased Fermi level observed by XPS. An effective standard correlating these two datasets quantitatively with carrier concentration or Fermi level is not available, but the results are consistent with the 400-meV shift observed by XPS and also confirm the EFM results, described below. The topographical response between domain lines up with the sMIM signals, indicating that the domain is the source of variation and verifying the ferroelectric nature of the material. As seen in the topography image, there is a distinct crack running through the domain, which is not present in the dC/dV signals, indicating that the sMIM response is due to the domain change, not topographical effects. There is no significant increase in carrier concentration around the domain walls, indicating that the walls are not relatively conductive and thus would not shunt a device.

In addition to the XPS and sMIM measurements, we investigated the domain-specific electrical response through EFM. We show that domains of differing orientations exhibit a measurably different electrical response. Figure 3 (D to F) shows the results of both the

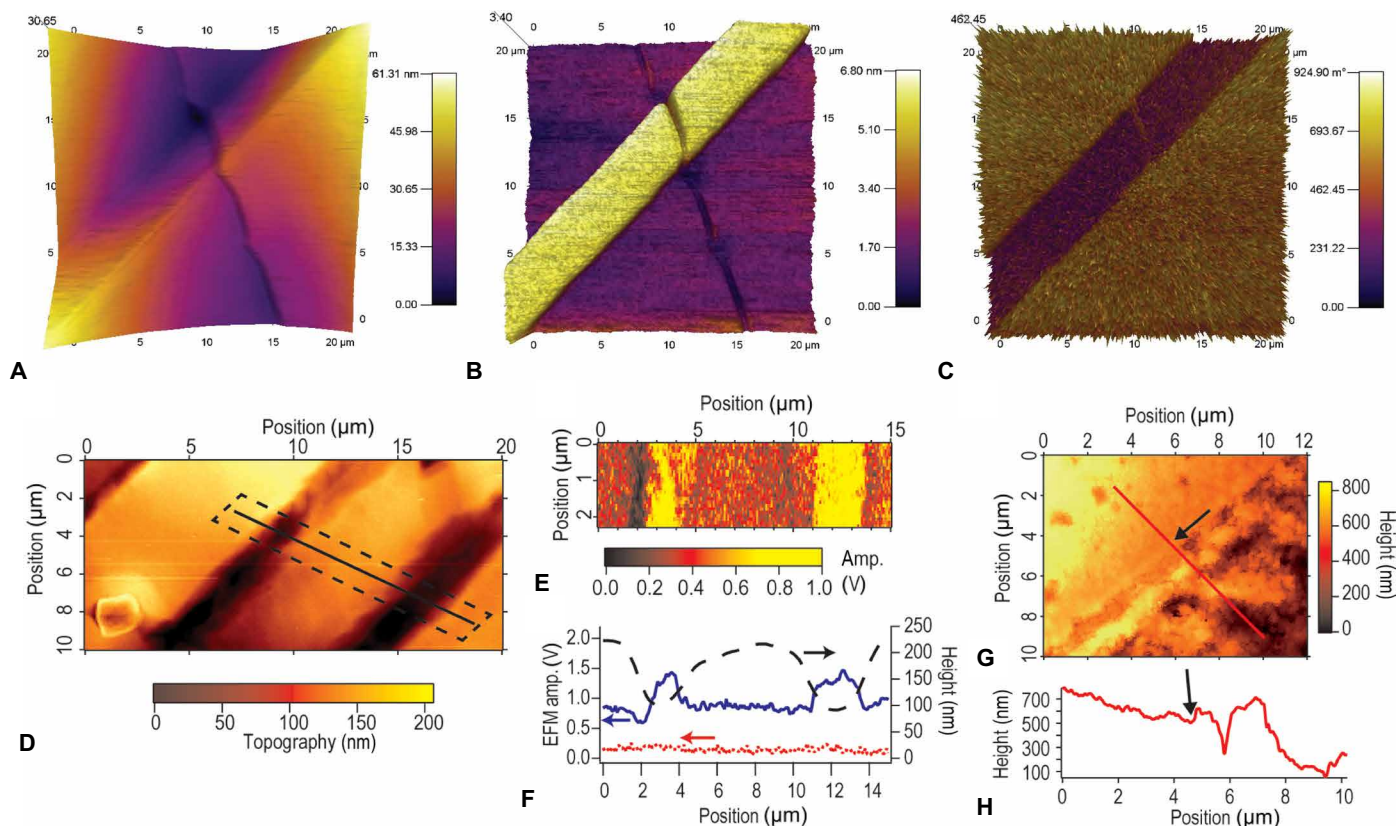


Fig. 3. Scanning microwave and electrical microscopy. (A) AFM topography image depicting distinct domain boundaries. (B) sMIM (dC/dV) amplitude showing increased signal within the positive domain, indicating decreased carrier concentration. (C) The positive domain displays decreased sMIM (dC/dV) phase, indicating a more n-type region. (D) The AFM topography of domain lines, where the area delineated by dashed line corresponds to the EFM amplitude scan area in (E) at 8 V bias. (F) Line scans corresponding to the black solid line in (D), showing the response for topography (dashed, black line, right axis), EFM amplitude signal at 0 V bias (red, dotted line, left axis) and 8 V (blue, solid line, left axis). (G) AFM topography image and line scan (H) after aging a poled crystal for 3 weeks in ambient.

topographical and EFM scans. The 0 V, 8 V, and topographical line scans are shown in Fig. 3F; the 0 V scan shows no response, verifying that the measured EFM signal is a function of a varied electrical response and not due to topographical features or surface chemical potential differences. In contrast, the 8 V scan shows a specific electrical response that is coincident with the domain structures. Although a complete analysis and understanding of the EFM response are beyond the scope of this work, it demonstrates domain-specific electrical response, which, in turn, implies that a built-in field can be engineered into working devices. Similar ferroelectric-induced electric fields have been shown to facilitate charge separation in other materials, indicating that domain engineering could improve photovoltaic performance.

The difference in chemical potential at the surface of different domains plays a large role in the stability of the material over time. The EFM/AFM images taken after a period of intentional etching in air for a month showed that domains in the dominant orientation remained relatively unchanged, while preferential etching and degradation occurred in domains with the opposite orientation. Etching occurs because of the humidity in the air reacting with the MAPbI₃ surface (14). This effect is shown in Fig. 3 (G and H), with the arrow indicating the domain boundary. While domain-specific etching and absorption are common in inorganic ferroelectric perovskites (15), these effects have not previously been reported in hybrid perovskites. By poling a crystal or film along this preferential direction,

the stability of the material could be increased. It is likely that poling could be optimized in future studies. Observing these phenomena in MAPbI₃ highlights a route to increase the stability and reliability of the material over time via targeted domain design.

DISCUSSION

Using a broad range of characterization techniques across multiple length scales, we have confirmed the existence of ferroelectric behavior in single crystals of MAPbI₃. To date, there are a number of conflicting reports on the presence of ferroelectricity in hybrid perovskites. One current prevailing view is that ferroelectricity does not or cannot occur in MAPbI₃ because of an inhibition of domain formation by charge screening, or the free rotation of the MA⁺ groups, or an intrinsic lack of spontaneous polarization (16–18). Others suggest that ferroelectricity can occur but is limited to temperatures below 50 K (19) or that an antiferroelectric configuration is preferable (20) or that the material is ferroelastic but not ferroelectric (21). Despite this, there are a number of DFT calculations, three-dimensional drift diffusion models, and Monte Carlo simulations that predict that ferroelectricity should occur in MAPbI₃ (22–24). In addition, there is a well-established precedence for ferroelectricity in perovskite-structured materials and a number of known inorganic and hybrid perovskite ferroelectrics (25). Experimental studies have come to conflicting consensus about the presence and persistence of

a ferroelectric response (16, 26, 27). Rakita *et al.* (27) observed a pyroelectric response and second-harmonic generation, indicating that the material has a polar structure (which is a prerequisite but not exclusive to a ferroelectric response). PFM results have previously been reported for MAPbI₃ thin films by Coll *et al.* (28), who reported a transient PFM response that exhibits similar hysteresis characteristics, but a lower magnitude for the piezoelectric response and without the claim of permanent ferroelectricity. Domain structures similar to those observed here have also been seen in MAPbI₃ thin films (29). Within that work, the reported changes in coercivity support a relaxor ferroelectric response, where the size and, thus, total ferroelectric response are sensitive to the frequency and applied electric field. Furthermore, identifying a ferroelectric response and showing polarization reorientation under electric field by single-frequency PFM in polycrystalline thin films are problematic due to the convolution of electrostatic, electrostrictive, and topographic contributions to the signal (5).

The presence of nanopolar regions of ferroelectricity, i.e., relaxor ferroelectricity, in single crystals of MAPbI₃ explains the discrepancies and disagreements within previous reports. Relaxors can mimic a ferroelectric or dipolar glass (a material with randomly oriented dipoles) depending on the field and temperature history and the spatial and temporal scales of the measurement (7). Relaxor ferroelectricity results from chemical, structural, or potential variations on the nanoscale, which are known to occur in hybrid materials (30). The residual amorphous material, grain boundaries, and secondary phases found in many hybrid thin films would further hinder ferroelectric measurements. One consequence of relaxor ferroelectricity in MAPbI₃ would be a large change in the electrical response of the material after any change in the local chemical inhomogeneity. In addition, since relaxor ferroelectrics can be poled into a macroscopic state, as we have shown, and because the coercive voltage for this is low, it is possible that material could see high enough voltages during operation to lead to further structural and electrical changes.

It has also been suggested that the rotation of the MA⁺ ions within the inorganic framework could inhibit ferroelectric ordering; however, recent quasi-elastic neutron scattering and Monte Carlo simulations have shown that the MA⁺ groups do not freely rotate but hop between equivalent positions oriented toward the cubic faces (31). This is akin to the dynamic dipole rotations in barium titanate, a prototypical ferroelectric, and lead magnesium niobate, a relaxor ferroelectric (32). Density functional perturbation theory calculations of the piezoelectric tensor for MAPbI₃ show an order of magnitude variation of d_{33} depending on the orientation of the MA⁺ ions. The calculated d_{33} ranges from a maximum of 32.8 pC/N when the MA⁺ ions are aligned in a polar configuration to a minimum of 2.9 pC/N when the MA⁺ ions are oppositely aligned in a nonpolar configuration. The similarity of the measured d_{33} with the calculated d_{33} for the polar configuration suggests that the MA⁺ ions are aligned in a polar configuration during the piezoelectric measurements, which is counter to most theories that suggest MA⁺ cation orientation is fully disordered at temperatures tested in this work. Allowing for a preferential orientation for the MA⁺ cation is fully commensurate with relaxor ferroelectric description of MAPbI₃ in which the reaction coordinate for the ferroelectric behavior is the relative order of the MA⁺ cation orientation.

Dipole doping in ferroelectric semiconductors is known to increase the V_{oc} , J_{sc} , and the fill factor of the photovoltaic response,

and it is likely that similar effects would contribute to the high efficiency in MAPbI₃ (1). It is also possible that the ferroelectric response could contribute to the J - V hysteresis observed in many MAPbI₃-based solar cells, although there are likely many other dominant contributors to this phenomenon. Domain engineering through poling of the nanopolar regions into macroscopic domains provides routes not only to increased stability and directional control of the electrical response in MAPbI₃ but also the potential to mitigate the ferroelectric contributions to hysteretic electrical properties.

An important implication of this work is that any ferroelectric semiconductor, such as MAPbI₃, can also exhibit the bulk photovoltaic effect (2). The bulk photovoltaic effect in ferroelectrics relies on the spontaneous polarization, which enables efficient separation of photo-excited charge carriers without a p-n junction. Ferroelectric photovoltaic absorbers have been reported to exceed the Shockley-Queisser limit (2). In addition, BPE devices can have a $V_{oc} >$ band-gap. The current record efficiency for a BPE device is 8.1%, but first principles calculations predict that if MAPbI₃ is ferroelectric, which we show here, then the BPE coefficient would be three times greater than the class of materials that are the current record holders (33). Previous reports of similar ferroelectric hybrid organic-inorganic halide perovskites have shown a BPE response with a V_{oc} of 32 V (34). Reports of giant photostriction and a giant switchable photovoltaic effect in MAPbI₃ are also suggestive of a BPE response (35). Within this, work we show that the MAPbI₃ is ferroelectric, that the polarization can be controlled through poling, and that the domain structure affects the optoelectronic response, three critical criteria for the development of BPE devices. These results support the idea that the BPE effect in MAPbI₃ may contribute to the spectacular photovoltaic response observed in this material.

The current work shows, through a variety of characterization techniques, the existence of relaxor ferroelectric behavior in single crystals of MAPbI₃. The application of uncommon techniques, such as d_{33} Berlincourt measurements, BE-PFM/cKPFM, Rayleigh analysis, and small-signal, large-area PFM have provided insight into the complex ferroelectric response of these hybrid organic-inorganic perovskite materials. Identifying nanopolar regions of ferroelectricity, i.e., relaxor ferroelectricity, helps to explain and resolve the persistent debate within previous reports. This work also demonstrates how to control the ferroelectricity response in MAPbI₃ and its influence on the optoelectronic response, such as measurable changes in Fermi level position, conductivity, response to an electrical probe, and the rate at which it degrades, suggesting that domain engineering is a viable route to increased performance and stability.

MATERIALS AND METHODS

Crystal growth, characterization, and preparation

Single crystals were prepared using an acid-initiated solution growth method similar to that previously reported (36). Briefly, iodide salt solutions at 0.8 M in 4 ml of fresh γ -butyrolactone were prepared by dissolving the salts at 55°C with vigorous stirring for at least 30 min. The solution was filtered with a 0.45- μ m syringe filter and placed in an oil bath at 95°C in a closed crystallization dish. After the initial seed growth, an appropriate seed crystal (~0.5 mm) was placed in a similarly prepared solution and allowed to grow for 10 to 12 hours. The process was repeated multiple times until the crystal was of an appropriate size for the characterization technique. For the poling and EFM measurements, a double-sided, conductive copper tape was

used to form an electrical connection between the crystal and a conducting substrate. This electric field was approximately 21 V/cm, but the local electric field could have varied due to differences in the contact with the removable electrodes. Future work should be able to optimize poling. For the Rayleigh analysis and PFM, 100-nm-thick gold electrodes, approximately 3 mm in diameter, were thermally evaporated on opposite facets of the crystal; electrical connection was made by adhering the bottom facet to a metalized substrate using silver paste and using a microprobe to contact the top electrode.

X-ray crystallography

Structures were determined for the compounds listed in table S1. Single crystals were coated with paratone-N oil and mounted under a cold stream of dinitrogen gas. Single-crystal x-ray diffraction data were acquired on a Bruker Kappa APEX II CCD diffractometer with Mo $K\alpha$ radiation ($\lambda = 0.71073 \text{ \AA}$) and a graphite monochromator. Initial lattice parameters were obtained from a least-squares analysis of more than 100 reflections; these parameters were later refined against all data. None of the crystals showed significant decay during data collection. Data were integrated and corrected for Lorentz and polarization effects using Bruker APEX3 software, and semiempirical absorption corrections were applied using SCALE (Sheldrick, G.M. SADABS – a program for area detector absorption corrections). Space group assignments were based on systematic absences, E statistics, and successful refinement of the structures. Structures were solved using Direct Methods and were refined with the aid of successive Fourier difference maps against all data using the SHELXTL 6.14 software package (Sheldrick, G.M. *SHELXTL*, v. 6.12; Bruker AXS: Madison, WI, 1999). Thermal parameters for all nonhydrogen atoms were refined anisotropically. All hydrogen atoms were assigned to ideal positions and refined using a riding model with an isotropic thermal parameter 1.2 times that of the attached carbon atom (1.5 times for methyl hydrogens).

Piezoresponse force microscopy

A 2-N/m platinum-coated tip (SCM-PIT-V2 Bruker) was used on a Bruker atomic force microscope system (Billerica, MA). During PFM measurements, an AC signal ranging from 20 up to 10 V was applied at 750 kHz. This frequency was chosen to avoid resonance. The single-frequency PFM measurements are taken at a rate of 0.1 Hz, averaged over 10 measurements each, and taken with a 20-ms delay between voltage steps. The response was measured quasi-statically on a well-defined gold top electrode. The response did not change over multiple sweeps taken over multiple days. Further quasi-static measurements were taken on the bare surface of the material, which showed a similar PFM response. Static scans remove the possibility of changes in topography, leading to a false phase signal. The use of small-signal measurements reduces the amount of injected charge and the possibility of large electrostrictive contributions, while using large electrodes averages over a wide range of material so the contributions of surface defects are reduced. All PFM and electrical measurements were taken with no illumination to reduce contributions from photogenerated carriers. For large signal measurements, the domain reorientation by poling was duplicated in an external LCR measurement system.

Band excitation piezoresponse force microscopy with contact Kelvin probe force microscopy

Here, band excitation PFM with contact Kelvin probe microscopy was performed using an Asylum Research AFM (Cypher) interfaced

with National Instruments data acquisition cards controlled by a Labview software at Oak Ridge National Laboratory–Center for Nanophase Material Science. Pt-coated tips (Budget Sensors ElectriMulti75-G; nominal resonance frequency, 75 kHz; nominal force constant, 3 N/m) were used to apply voltages to the sample. Band excitation uses a digitally synthesized frequency pulse with a finite spectral density, rather than sending a single-frequency pulse as is typically done in single-frequency PFM (6). A 10 \times amplifier was used in all BE-PFM/cKPFM measurements. The frequency range of the band excitation was centered at 320 kHz, and the BE-PFM excitation was 2.5 V. The measurements were taken over a grid of 10 by 10 points on the sample surface for an averaged response. For the cKPFM measurements, a DC write voltage was applied stepwise from 0 \rightarrow 15 V \rightarrow –15 V \rightarrow 0 V, in intervals of 2.13 V for a total of 128 steps. These voltage pulses are referred to as the write steps. Interspersed between every write step is a read step, where the piezoresponse and cKPFM response are measured from –2 V \rightarrow 2 V in a total of seven steps. The delay time between subsequent measurements is in the milliseconds. The piezoresponse measured at 0 V during the read measurements is shown in the off-field response. The voltage-dependent response is determined from a fit of the band excitation data to a simple harmonic oscillator model, described in (6). From this analysis, the oscillation amplitude, phase, resonance frequency, and quality factor are extracted. The measurements were taken over a grid of 10 by 10 points on the sample surface to give the averaged response reported here, and this measurement was repeated on four samples with consistent results. The resulting response was repeatable and persisted unchanging over the course of the experiment (4 days). All measurements were taken in the dark.

Electrical force microscopy

The single crystals were mounted on an AFM sample holder via a conducting double-sided copper tape. The top surface of the crystal was exposed to a high voltage (i.e., poled) to facilitate ferroelectric domain formation (described in detail elsewhere). This electric field was approximately 21 V/cm, but the local electric field could have varied due to differences in the contact with the removable electrodes. It is likely that poling could be optimized in future studies. The EFM measurements were performed under ambient conditions using single-pass mode on a Park AFM equipped with an XE-70 controller and an external lock-in amplifier (SR830, Stanford Research Systems). The external lock-in amplifier was used for electrical AC bias of the tip, lock-in detection, and feedback at 18 kHz of the EFM signal. Conductive Pt/Ir-coated AFM tips (Multi-75EG, Budget Sensors) were used for the measurements. Topography was measured at the first resonance frequency (\sim 75 kHz), and EFM was collected with a 1.00 V_{AC} bias at 18 kHz, well separated from the topography frequency. The scan rate was 0.1 Hz. Surface topography and EFM were mapped simultaneously while varying the sample bias voltages (0 to \pm 10 V).

Scanning microwave impedance microscopy

sMIM capacitive measurements were taken on an Asylum Research MFP-3D AFM using PrimeNano's ScanWave technology (37). Single crystals with bottom electrodes were mounted on a grounded sample stage, and scans were conducted under ambient conditions. Shielded, coaxial cantilever probes with TiW tips were used to perform measurements (ScanWave M300S). A 6.0 V_{DC} bias was applied to the probe tip, and a lock-in amplifier was used to add a 4.0 V_{AC}

signal at a frequency of 200 kHz. These values were determined through experimentation to maximize the sMIM signal strength. At the same time, a 3.0-GHz microwave signal was sent through the tip and into the sample. The scan rate was 1.0 Hz, and topography was mapped in conjunction with capacitance data. Carrier concentration and carrier type are measured by calculating the change in capacitance with respect to the AC tip voltage, dC/dV . The dC/dV signal amplitude is proportional to carrier concentration, while the phase of the signal represents carrier type.

Electrical measurements

The dielectric temperature and frequency dependence and Rayleigh behavior were measured using a precision LCR meter (Hewlett Packard 4284A, Palo Alto, CA). The heating and cooling rates were controlled by a Peltier heater, monitored by a type K thermocouple, which was read via a digital multimeter (Hewlett Packard 3478). Samples were allowed to equilibrate for 2 min prior to taking a measurement. Rayleigh behavior was characterized at 1 MHz. No changes were observed in the Rayleigh response upon multiple cycles of applied AC electric fields, indicating that the response was not induced or affected by the application of this electric field. The temperature of the global phase transition temperature occurs at the same temperature for increasing and decreasing temperature sweeps within the limit of the experimental step size. Further information on the Rayleigh analysis methodology for indicating residual ferroelectricity can be found in (8). Polarization–electric field measurements were taken on a Precision Multiferroic materials analyzer (Radiant Technologies Inc., Albuquerque, NM).

Berlincourt d_{33} measurements

Piezoelectric measurements were conducted on a wide-range Berlincourt d_{33} meter (APC International Ltd.) piezoelectric coefficient. Poling for the d_{33} Berlincourt measurements was conducted on a precision LCR meter (Hewlett Packard 4284A, Palo Alto, CA) at approximately 21 V/cm for 5 min.

DFT calculations

First principles calculations were performed using the projector augmented wave method (38) as implemented in the Vienna Ab Initio Simulation Package (39). Structures were relaxed using the standard parameters of the Materials Project (40). Density functional perturbation calculations using the Perdew–Becke–Ernzerhof (41) generalized gradient approximation for the exchange–correlation functional, a plane wave cutoff of 1000 eV, and a k -point density of approximately 2000 per reciprocal atom were used to calculate the piezoelectric tensor. The elastic tensor was computed in DFT with a plane wave cutoff of 700 eV and a k -point density of 7000 per reciprocal atom using explicit perturbations of the lattice corresponding to the six principle deformations and fit assuming a linear relationship. The reported piezoelectric tensor was then computed by the dot product of the piezoelectric stress tensor computed via DFT and the computed compliance tensor. Part of the difference between the theory and measurements could stem from the lack of inclusion of van der Waals interactions in the DFT calculations, temperature differences, or underrepresenting the contribution from the molecular ferences. Furthermore, we calculate the remanent piezoresponse as partial derivative with respect to strain and electric field. This is very sensitive to any tiny changes around the zero response, so having 60% of the experimental value is a reasonable approximation.

X-ray photoemission spectroscopy

Photoemission spectroscopy measurements were performed on a Kratos NOVA spectrometer calibrated to the Fermi edge and core level positions of sputter-cleaned metal (Au, Ag, Cu, and Mo) surfaces. X-ray photoemission spectra were taken using monochromated Al $K\alpha$ radiation (1486.7 eV) at a resolution of 400 meV and fit using pseudo-Voigt profiles. Spectral acquisition followed the precautions laid out in (42) without light bias and using low x-ray fluences at nominal 1.5-W anode power. XPS measurements were conducted on the (100) surface of the poled and unpoled MAPbI₃ crystals. To acquire the relevant MAPbI₃ core level spectra, the copper foil tape used as the top electrode for poling the single crystal has been removed in air prior to introducing the crystal into vacuum to perform the XPS experiment. The same procedure has been applied to the unpoled single crystal. The existence, or respectively absence, of macroscopic domains has been verified by optical microscopy for each sample before moving the crystal into the vacuum chamber. There is a precedence for the observation of core level shifts in a ferroelectric due to the poling of a ferroelectric from the XPS work on BaTiO₃ single crystals (43).

SUPPLEMENTARY MATERIALS

Supplementary material for this article is available at <http://advances.sciencemag.org/cgi/content/full/5/1/eaas9311/DC1>

Table S1. Single crystal x-ray diffraction indexing results.

Fig. S1. BE-PFM raw data.

Fig. S2. The extracted piezoresponse.

Fig. S3. The piezoresponse extracted from the BE-PFM measurements averaged over a matrix of 10 by 10 points.

Fig. S4. The single-frequency PFM small-signal amplitude (black) and phase response (blue) for a trace and a retrace.

Fig. S5. Rayleigh analysis and loss for single-crystal MAPbI₃ at 1 MHz.

Fig. S6. Optical microscope images of the surface of a MAPbI₃ single crystal before poling.

References (44, 45)

REFERENCES AND NOTES

1. K. S. Nalwa, J. A. Carr, R. C. Mahadevapuram, H. K. Kodali, S. Bose, Y. Chen, J. W. Petrich, B. Ganapathysubramanian, S. Chaudhary, Enhanced charge separation in organic photovoltaic films doped with ferroelectric dipoles. *Energ. Environ. Sci.* **5**, 7042–7049 (2012).
2. J. E. Spanier, V. M. Fridkin, A. M. Rappe, A. R. Khabashev, A. Polemi, Y. Qi, Z. Gu, S. M. Young, C. J. Hawley, D. Imbrenda, G. Xiao, A. L. Bennett-Jackson, C. L. Johnson, Power conversion efficiency exceeding the Shockley–Queisser limit in a ferroelectric insulator. *Nat. Photonics* **10**, 611–616 (2016).
3. M. A. Green, K. Emery, Y. Hishikawa, W. Warta, E. D. Dunlop, Solar cell efficiency tables (version 48). *Progr. Photovolt.* **24**, 905–913 (2016).
4. M. E. Lines, A. M. Glass, *Principles and Applications of Ferroelectrics and Related Materials* (Oxford Univ. Press, Oxford, UK, ed. 1, 1977).
5. N. Balke, P. Maksymovych, S. Jesse, A. Herklotz, A. Tselev, C.-B. Eom, I. I. Kravchenko, P. Yu, S. V. Kalinin, Differentiating ferroelectric and nonferroelectric electromechanical effects with scanning probe microscopy. *ACS Nano* **9**, 6484–6492 (2015).
6. S. Jesse, R. K. Vasudevan, L. Collins, E. Strelcov, M. B. Okatan, A. Belianinov, A. P. Baddorf, R. Proksch, S. V. Kalinin, Band excitation in scanning probe microscopy: Recognition and functional imaging. *Annu. Rev. Phys. Chem.* **65**, 519–536 (2014).
7. L. E. Cross, Relaxor ferroelectrics. *Ferroelectrics* **76**, 241–267 (1987).
8. L. M. Garten, M. Burch, A. S. Gupta, R. Haislmaier, V. Gopalan, E. C. Dickey, S. Trolier-McKinstry, Relaxor ferroelectric behavior in barium strontium titanate. *J. Am. Ceram. Soc.* **99**, 1645–1650 (2016).
9. L. T. Schelhas, J. A. Christians, J. J. Berry, M. F. Toney, C. J. Tassone, J. M. Luther, K. H. Stone, Monitoring a silent phase transition in CH₃NH₃PbI₃ solar cells via *operando* X-ray diffraction. *ACS Energy Lett.* **1**, 1007–1012 (2016).
10. M. A. Khan, M. A. Nadeem, H. Idriss, Ferroelectric polarization effect on surface chemistry and photo-catalytic activity: A review. *Surf. Sci. Rep.* **71**, 1–31 (2016).
11. Y. Yuan, Z. Xiao, B. Yang, J. Huang, Arising applications of ferroelectric materials in photovoltaic devices. *J. Mater. Chem. A* **2**, 6027–6041 (2014).

12. P. Schulz, E. Edri, S. Kirmayer, G. Hodes, D. Cahen, A. Kahn, Interface energetics in organo-metal halide perovskite-based photovoltaic cells. *Energ. Environ. Sci.* **7**, 1377–1381 (2014).
13. K. X. Steirer, P. Schulz, G. Teeter, V. Stevanovic, M. Yang, K. Zhu, J. J. Berry, Defect tolerance in methylammonium lead triiodide perovskite. *ACS Energy Lett.* **1**, 360–366 (2016).
14. T. Leijtens, G. E. Eperon, N. K. Noel, S. N. Habisreutinger, A. Petrozza, H. J. Snaith, Stability of metal halide perovskite solar cells. *Adv. Energy Mater.* **5**, 1500963 (2015).
15. C. L. Sones, S. Mails, W. S. Brocklesby, R. W. Eason, J. R. Owen, Differential etch rates in z-cut LiNbO₃ for variable HF/HNO₃ concentrations. *J. Mater. Chem.* **12**, 295–298 (2002).
16. Z. Fan, J. Xiao, K. Sun, L. Chen, Y. Hu, J. Ouyang, K. P. Ong, K. Zeng, J. Wang, Ferroelectricity of CH₃NH₃PbI₃ Perovskite. *J. Phys. Chem. Lett.* **6**, 1155–1161 (2015).
17. S. Govinda, P. Mahale, B. P. Kore, S. Mukherjee, M. S. Pavan, C. De, S. Ghara, A. Sundaresan, A. Pandey, T. N. Guru Row, D. D. Sarma, Is CH₃NH₃PbI₃ polar? *J. Phys. Chem. Lett.* **7**, 2412–2419 (2016).
18. M. N. F. Hoque, M. Yang, Z. Li, N. Islam, X. Pan, K. Zhu, Z. Fan, Polarization and dielectric study of methylammonium lead iodide thin film to reveal its nonferroelectric nature under solar cell operating conditions. *ACS Energy Lett.* **1**, 142–149 (2016).
19. A. Filippetti, P. Delugas, M. I. Saba, A. Mattoni, Entropy-suppressed ferroelectricity in hybrid lead-iodide perovskites. *J. Phys. Chem. Lett.* **6**, 4909–4915 (2015).
20. G. A. Sewvandi, D. Hu, C. Chen, H. Ma, T. Kusunose, Y. Tanaka, S. Nakanishi, Q. Feng, Antiferroelectric-to-ferroelectric switching in CH₃NH₃PbI₃ perovskite and its potential role in effective charge separation in perovskite solar cells. *Phys. Rev. Appl.* **6**, 024007 (2016).
21. E. Strelcov, Q. Dong, T. Li, J. Chae, Y. Shao, Y. Deng, A. Gruverman, J. Huang, A. Centrone, CH₃NH₃PbI₃ perovskites: Ferroelasticity revealed. *Sci. Adv.* **3**, e1602165 (2017).
22. T. S. Sherkar, L. J. A. Koster, Can ferroelectric polarization explain the high performance of hybrid halide perovskite solar cells? *Phys. Chem. Chem. Phys.* **18**, 331–338 (2016).
23. S. Liu, F. Zheng, N. Z. Koocher, H. Takenaka, F. Wang, A. M. Rappe, Ferroelectric domain wall induced band gap reduction and charge separation in organometal halide perovskites. *J. Phys. Chem. Lett.* **6**, 693–699 (2015).
24. J. M. Frost, K. T. Butler, A. Walsh, Molecular ferroelectric contributions to anomalous hysteresis in hybrid perovskite solar cells. *APL Mater.* **2**, 081506 (2014).
25. N. Setter, D. Damjanovic, L. Eng, G. Fox, S. Gevorgian, S. Hong, A. Kingon, H. Kohlstedt, N. Y. Park, G. B. Stephenson, I. Stolitchnov, A. K. TagansteV, D. V. Taylor, T. Yamada, S. Streiffner, Ferroelectric thin films: Review of materials, properties, and applications. *J. Appl. Phys.* **100**, 051606 (2006).
26. J. Wei, Y. Zhao, H. Li, G. Li, J. Pan, D. Xu, Q. Zhao, D. Yu, Hysteresis analysis based on the ferroelectric effect in hybrid perovskite solar cells. *J. Phys. Chem. Lett.* **5**, 3937–3945 (2014).
27. Y. Rakita, O. Bar-Elli, E. Meirzadeh, H. Kaslasi, Y. Peleg, G. Hodes, I. Lubomirsky, D. Oron, D. Ehre, D. Cahen, Tetragonal CH₃NH₃PbI₃ is ferroelectric. *Proc. Natl. Acad. Sci. U.S.A.* **114**, E5504–E5512 (2017).
28. M. Coll, A. Gomez, E. Mas-Marza, O. Almora, G. Garcia-Belmonte, M. Campoy-Quiles, J. Bisquert, Polarization switching and light-enhanced piezoelectricity in lead halide perovskites. *J. Phys. Chem. Lett.* **6**, 1408–1413 (2015).
29. H. Röhm, T. Leonhard, M. J. Hoffmann, A. Colsmann, Ferroelectric domains in methylammonium lead iodide perovskite thin-films. *Energ. Environ. Sci.* **10**, 950–955 (2017).
30. B. P. Burton, E. Cockayne, U. V. Waghmare, Correlations between nanoscale chemical and polar order in relaxor ferroelectrics and the lengthscale for polar nanoregions. *Phys. Rev. B* **72**, 064113 (2005).
31. A. M. A. Leguy, J. M. Frost, A. P. McMahon, V. G. Sakai, W. Kochelmann, C. Law, X. Li, F. Foglia, A. Walsh, B. C. O'Regan, J. Nelson, J. T. Cabral, P. R. F. Barnes, The dynamics of methylammonium ions in hybrid organic–inorganic perovskite solar cells. *Nat. Commun.* **6**, 7124 (2015).
32. R. Pirc, R. Blinc, Off-center Ti model of barium titanate. *Phys. Rev. B* **70**, 134107 (2004).
33. F. Zheng, H. Takenaka, F. Wang, N. Z. Koocher, A. M. Rappe, First-principles calculation of the bulk photovoltaic effect in CH₃NH₃PbI₃ and CH₃NH₃PbI_{3-x}Cl_x. *J. Phys. Chem. Lett.* **6**, 31–37 (2015).
34. H.-Y. Ye, Y. Zhang, D.-W. Fu, R.-G. Xiong, An above-room-temperature ferroelectric organo-metal halide perovskite: (3-pyrrolinium)(CdCl₃). *Angew. Chem. Int. Ed.* **53**, 11242–11247 (2014).
35. Y. Zhou, L. You, S. Wang, Z. Ku, H. Fan, D. Schmidt, A. Rusydi, L. Chang, L. Wang, P. Ren, L. Chen, G. Yuan, L. Chen, J. Wang, Giant photostriction in organic–inorganic lead halide perovskites. *Nat. Commun.* **7**, 11193 (2016).
36. P. K. Nayak, D. T. Moore, B. Wenger, S. Nayak, A. A. Haghighirad, A. Fineberg, N. K. Noel, O. G. Reid, G. Rumbles, P. Kukura, K. A. Vincent, H. J. Snaith, Mechanism for rapid growth of organic–inorganic halide perovskite crystals. *Nat. Commun.* **7**, 13303 (2016).
37. K. Lai, W. Kundhikanjana, M. A. Kelly, Z.-X. Shen, Nanoscale microwave microscopy using shielded cantilever probes. *Appl. Nanosci.* **1**, 13–18 (2011).
38. G. Kresse, D. Joubert, From ultrasoft pseudopotentials to the projector augmented-wave method. *Phys. Rev. B* **59**, 1758–1775 (1999).
39. G. Kresse, J. Furthmüller, Efficient iterative schemes for ab initio total-energy calculations using a plane-wave basis set. *Phys. Rev. B* **54**, 11169–11186 (1996).
40. A. Jain, S. P. Ong, G. Hautier, W. Chen, W. D. Richards, S. Dacek, S. Cholia, D. Gunter, D. Skinner, G. Ceder, K. A. Persson, Commentary: The Materials Project: A materials genome approach to accelerating materials innovation. *APL Mater.* **1**, 011002 (2013).
41. J. P. Perdew, K. Burke, M. Ernzerhof, Generalized gradient approximation made simple. *Phys. Rev. Lett.* **77**, 3865–3868 (1996).
42. R. L. Z. Hoye, P. Schulz, L. T. Schelhas, A. M. Holder, K. H. Stone, J. D. Perkins, D. Vigil-Fowler, S. Siol, D. O. Scanlon, A. Zakutayev, A. Walsh, I. C. Smith, B. C. Melot, R. C. Kurchin, Y. Wang, J. Shi, F. C. Marques, J. J. Berry, W. Tumas, S. Lany, V. Stevanovic, M. F. Toney, T. Buonassisi, Perovskite-inspired photovoltaic materials: Toward best practices in materials characterization and calculations. *Chem. Mater.* **29**, 1964–1988 (2017).
43. F. Chen, A. Klein, Polarization dependence of Schottky barrier heights at interfaces of ferroelectrics determined by photoelectron spectroscopy. *Phys. Rev. B* **86**, 094105 (2012).
44. Y. Yuan, J. Chae, Y. Shao, Q. Wang, Z. Xiao, A. Centrone, J. Huang, Photovoltaic switching mechanism in lateral structure hybrid perovskite solar cells. *Adv. Energy Mater.* **5**, 1500615 (2015).
45. T. Leijtens, E. T. Hoke, G. Grancini, D. J. Slotcavage, G. E. Eperon, J. M. Ball, M. De Bastiani, A. R. Bowring, N. Martino, K. Wojciechowski, M. D. McGehee, H. J. Snaith, A. Petrozza, Mapping electric field-induced switchable poling and structural degradation in hybrid lead halide perovskite thin films. *Adv. Energy Mater.* **5**, 1500962 (2015).

Acknowledgments: This work was funded by the Center for the Next Generation of Materials by Design, a U.S. Department of Energy, Office of Science EFRC, under contract no. DE-AC36-08GO28308 to NREL. D.T.M. acknowledges support from the NREL Director's Fellowship LDRD program. We acknowledge S. Neumayer and S. Jesse (ORNL) for facilitating the Be-PFM/cKPFM measurements conducted at the Center for Nanophase Materials Sciences, which is a DOE Office of Science User Facility. S.T.M. gratefully acknowledges the NSF (DMR-1420620). A.R. and J.W. acknowledge support under the Department of Energy grant DE-EE0007545. P.S. thanks the French Agence Nationale de la Recherche for funding under contract number ANR-17-MPGA-0012 and was supported by the hybrid perovskite solar cell program of the National Center for Photovoltaics funded by the U.S. Department of Energy, Office of Energy Efficiency and Renewable Energy, Office of Solar Energy Technology under award number DE-AC36-08GO28308DOE with NREL. **Author contributions:** L.M.G. designed the study. D.T.M. grew the samples. L.M.G. conducted the electrical and PFM measurements, and L.M.G. and S.T.-M. analyzed these measurements. L.M.G. conducted the BE-PFM/cKPFM. D.T.M. and S.N. performed the EFM/AFM. J.W. and A.R. performed and analyzed the sMIM. S.D. and K.A.P. performed the DFT piezoelectric and structure calculations. P.S. conducted the polarization-dependent XPS. B.N. conducted the x-ray diffraction. D.S.G., and S.T.-M. supervised the project. L.G. wrote the paper with support from D.M., K.A.P., S.T.-M., and D.S.G. All the authors approved the final paper for submission. **Competing interests:** D.S.G., L.M.G., and D.T.M. are inventors on a patent application related to this work (U.S. patent application no. 2018/0277695; PCT patent application publication no. WO 2018/175963). All the other authors declare that they have no competing interests. **Data and materials availability:** All data needed to evaluate the conclusions in the paper are present in the paper and/or the Supplementary Materials. Additional data related to this paper may be requested from the authors.

Submitted 5 January 2018

Accepted 7 December 2018

Published 25 January 2019

10.1126/sciadv.aas9311

Citation: L. M. Garten, D. T. Moore, S. U. Nanayakkara, S. Dwaraknath, P. Schulz, J. Wands, A. Rockett, B. Newell, K. A. Persson, S. Trolrier-McKinstry, D. S. Ginley, The existence and impact of persistent ferroelectric domains in MAPbI₃. *Sci. Adv.* **5**, eaas9311 (2019).

The existence and impact of persistent ferroelectric domains in MAPbI₃

Lauren M. Garten, David T. Moore, Sanjini U. Nanayakkara, Shyam Dwaraknath, Philip Schulz, Jake Wands, Angus Rockett, Brian Newell, Kristin A. Persson, Susan Trolier-McKinstry and David S. Ginley

Sci Adv 5 (1), eaas9311.
DOI: 10.1126/sciadv.aas9311

ARTICLE TOOLS	http://advances.sciencemag.org/content/5/1/eaas9311
SUPPLEMENTARY MATERIALS	http://advances.sciencemag.org/content/suppl/2019/01/18/5.1.eaas9311.DC1
REFERENCES	This article cites 44 articles, 2 of which you can access for free http://advances.sciencemag.org/content/5/1/eaas9311#BIBL
PERMISSIONS	http://www.sciencemag.org/help/reprints-and-permissions

Use of this article is subject to the [Terms of Service](#)

Science Advances (ISSN 2375-2548) is published by the American Association for the Advancement of Science, 1200 New York Avenue NW, Washington, DC 20005. 2017 © The Authors, some rights reserved; exclusive licensee American Association for the Advancement of Science. No claim to original U.S. Government Works. The title *Science Advances* is a registered trademark of AAAS.